Nanoscale

PAPER

View Article Online
View Journal | View Issue

Cite this: *Nanoscale*, 2025, **17**, 864

Electrode informatics accelerated the optimization of key catalyst layer parameters in direct methanol fuel cells†

Lishou Ban,‡[a] Danyang Huang,‡[a] Yanyi Liu,‡[a] Pengcheng Liu,[a] Xihui Bian,[b] Kaili Wang,[c] Yifan Liu,*[d] Xijun Liu *[e] and Jia He*[a]

Received 21st July 2024,
Accepted 11th November 2024

DOI: 10.1039/d4nr03026e

rsc.li/nanoscale

As the core component of direct methanol fuel cells, the catalyst layer plays the key role as a species, proton and electron transport channel. However, due to the complexity of the system, optimizing its performance involves a large number of experiments and high costs. In this study, finite element simulation combined with machine learning model was constructed to accelerate power density prediction and evaluate the influence of catalyst layer parameters on the maximum power density of direct methanol fuel cells. We built a fuel cell simulation model corresponding to different parameters, obtaining a database of more than 200 sets of 19 eigenvalues, and then used different machine learning models for training and prediction. Finally, three tree-integration methods were selected to rank the importance of 19 characteristic parameters. In addition, we performed a high-throughput screening of 200 000 different parameter combinations based on sequential model-based algorithm configuration. We selected the top 10 parameter combinations with high expected improvement scores and employed them into a numerical simulation model. The results show that a majority of the polarization curves obtained from the top combinations exceed the maximum power density of the original database. This method greatly saves the time of collecting fuel cell data for experiments and speeds up the parameter optimization process.

1 Introduction

As a device that converts chemical energy directly into electrical energy, fuel cells have the advantages of high efficiency and environmental protection.[1–4] Among fuel cells, hydrogen-related proton-exchange membrane fuel cell is one of the important types.[5] However, before the application of hydrogen fuel cells, problems related to hydrogen production, hydrogen storage, and hydrogen transportation need to be solved, which brings development opportunities for methanol fuel cells.[6] Among them, direct methanol fuel cell (DMFC) has the characteristics of direct fuel injection into the stack, simple cell structure, and high cell energy density.[7–10] In the membrane electrode assembly, the catalyst layer (CL) is the core component, and its performance has a great influence on the output power density of the electrode in DMFC. Therefore, optimizing the CL design parameters of DMFC is crucial to improve its power density and overall performance.[11,12] At the physical level, factors such as catalyst loading,[21] ionomer ratio,[22] and humidity[23] play key roles in fuel cell performance. It is also of great significance to study the parameters that affect the operation of DMFC for the efficient and sustainable operation of DMFC.[13–20] Operating parameters such as temperature, backpressure, and reactant flow rates further increase the complexity of the parameter space. This means that the development of efficient electrode designs for DMFCs needs the integration of multiple aspects of effort. Experiments involving too many factors can also lead to confounding of the test criteria. Therefore, it is extremely difficult to draw general rules from these complex data. To address the above challenge, a suitable tool is required to draw effective conclusions from a large number of interrelated and mutually affecting factors to guide the design of electrodes for DMFC.

Numerical modelling has played a crucial role in recent research related to DMFCs as it allows for the modification of

[a]*School of Chemistry and Chemical Engineering, Institute for New Energy Materials & Low-Carbon Technologies, School of Materials Science and Engineering, Tianjin University of Technology, Tianjin 300384, China. E-mail: hejia1225@126.com*
[b]*State Key Laboratory of Separation Membranes and Membrane Processes, School of Chemical Engineering and Technology, Tiangong University, Tianjin 300387, China*
[c]*School of Chemistry, Chemical Engineering and Environmental Engineering, Weifang University, Weifang 261061, China*
[d]*Suzhou Laboratory, Suzhou 215100, China. E-mail: sparkle06@163.com*
[e]*MOE Key Laboratory of New Processing Technology for Nonferrous Metals and Materials, Guangxi Key Laboratory of Processing for Non-ferrous Metals and Featured Materials, School of Resources, Environment and Materials, Guangxi University, Nanning, 530004 Guangxi, China. E-mail: xjliu@gxu.edu.cn*

†Electronic supplementary information (ESI) available. See DOI: https://doi.org/10.1039/d4nr03026e

‡These authors contributed equally to this work.

relevant parameters to understand and predict the behaviour and performance of fuel cells. A variety of DMFC models has been developed to better understand the performance of DMFC under different conditions. For example, Yang *et al.*[24] combined theoretical and empirical models to establish a semi-empirical model that describes the relationship between the operating parameters, such as temperature, methanol concentration, methanol and air flow rates, and the performance of DMFCs. The model is sufficiently accurate to estimate the system performance and is suitable to investigate the DMFC degradation mechanism. Yu *et al.*[25] established a single-phase three-dimensional computational fluid dynamics (CFD) model to study the effects of channel geometry and operating parameters on DMFC performance. In addition, the model also has the potential for geometric parameter optimization design and operational parameter optimization control to develop DMFC systems. Tafaoli-Masoule[26] proposed a quasi-two-dimensional isothermal model for DMFCs to obtain the power exponent as the fitness function of a genetic algorithm and used genetic algorithms to determine the optimal parameters for maximizing the power of a single-cell DMFC. The optimal values of the DMFC cell temperature, anode and cathode pressure and channel height were determined to be 130 °C, 2.5 bar, 5 bar and 1 mm, respectively. Lee *et al.*[27] proposed an active DMFC system model that combines a one-dimensional DMFC stack model with major system components. The effects of DMFC operating parameters and thermal management were analysed through numerical modelling and simulations. The model determined that 0.6 M is the optimal methanol feed concentration to achieve the highest stack performance and also revealed the influence of ambient temperature and anode inlet temperature. Jiang *et al.*[28] proposed a two-phase two-dimensional model for DMFC with an ordered structure cathode CL, considering water accumulation around the cylindrical carbon nanowires in oxygen radial transport. The results show that DMFC with ordered electrodes can produce better cell performance. The above research results indicate that the application of numerical simulation in DMFCs has been very extensive, and it can gradually reveal the influence of many complex physical fields on the performance of DMFCs and provide guidance for the design of electrodes. However, numerical simulation also has the disadvantages of large amount of calculation, long time-consuming, and high computational cost. Moreover, if researchers want to study the relationship between different parameters and optimize a series of parameters at the same time, numerical simulation is particularly difficult.

Machine learning (ML), as a data-driven technique based on limited data and model training, has the potential to solve this problem. ML can obtain a certain data fitting model on the basis of existing data, revealing the hidden rules behind the input characteristics and output of the target system, such as image recognition driven by deep learning network,[29] personal recognition,[30] and automatic driving.[31] The complexity of DMFC also provides a suitable place for data-driven modelling. At present, the M model has been successfully applied to performance prediction, aging prediction and fault diagnosis of fuel cells and has obtained good accuracy in solving nonlinear problems. Combined with the optimization algorithm, the ML model can further optimize the design and operating parameters to achieve multiple optimization goals with good accuracy and efficiency.[32–39] For example, Liu *et al.*[40] designed an AI-based NPME auxiliary model for proton-exchange membrane fuel cell, which can well predict and analyse the maximum output power density and polarization curve by training with real experimental data in the literature. Ding *et al.*[41] trained nine different ML algorithms on experimental datasets in the laboratory to accurately predict performance and Pt utilization (Max R^2 = 0.973/0.968). The black-box interpretation method is applied to provide reliable insights into the optimal synthesis conditions from both qualitative and quantitative perspectives. Under the guidance of ML results, the ionomer/catalyst ratio, water content, organic solvent, catalyst load, stirring mode, solid content and ultrasonic spraying flow rate were optimized. The utilization rate of platinum is 0.147 g Pt kW^{-1} and the power density is 1.02 W cm^{-2}. The above research work shows that compared with numerical simulation technology, data-driven technology occupies much less time and computational resources and has a high degree of versatility. However, due to the complex structure and spatial characteristics of DMFC system electrodes, it is challenging to build a directly coupled electrode model by numerical simulation. Combining ML with numerical modelling is a promising method to improve the model accuracy and speed up the simulation process. This combination helps to better understand and predict the behaviour of complex systems, providing stronger support for scientific research and engineering practice.

In this paper, a 3D MEA model of DMFC is firstly established, and the influence of key parameters affecting CL on DMFC performance is discussed. The model consists of an anode/cathode flow channel, an anode/cathode diffusion layer, an anode/cathode CL, and a proton-exchange membrane that work together to achieve efficient energy conversion in DMFC. The model follows the mass conservation equation, momentum conservation equation and charge conservation equation, and the established model can clearly show the mass transfer process of the inlet and outlet flow channels and membrane electrodes of the fuel cell. Then, the different parameters of CL are calculated as input parameters, and the power density is used as the output parameter to establish the database. Regression models were built using 7 different ML algorithms to assess the importance of each parameter. Finally, precise combined data for predicting the output performance were obtained and calculated using the simulation model to obtain the *I–V* polarization curve and maximum power density, which were then compared with the data in the database. Scheme 1 describes the main aspects of the work. The results show that more than half of the polarization curves obtained from the top 10 parameter combinations with expected improvement (EI) score exceed the maximum power density of the original data. Therefore, the combination of numerical simulation and

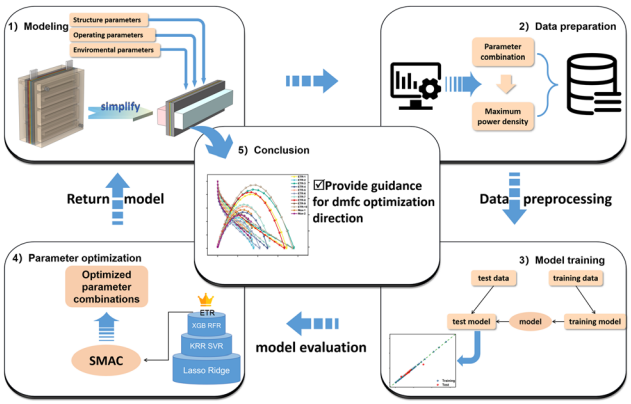

Scheme 1 Simulation and data dual-drive parameter optimization process.

machine learning can greatly save the time of collecting fuel cell data for experiments and accelerate the parameter optimization process.

2 Methods

2.1 DMFC numerical model

2.1.1 Physical field setting and boundary condition setting. We developed a three-dimensional steady-state multiphysics coupling model for DMFCs to study mass transfer, including anode and cathode flow channels, GDL, CL, and Nafion membranes. Several simplifying assumptions are introduced into the model.

(1) DMFC operates under steady-state conditions.

(2) The cross methanol from anode to cathode is completely oxidized by oxygen in the cathode CL.

(3) GDL, CL and membrane have isotropic permeability and effective porosity.

(4) The electrochemical reaction is complete, with only CO_2 and H_2O being produced.

(5) The flow is laminar, both fully developed and incompressible.

(6) A mixture of reaction gases is considered ideal.

(7) The process is isothermal.

(8) Gravity effects are ignored.

(9) The catalytic layer and diffusion layer of the anode and the cathode have the same diffusivity and other characteristic parameters. The effects of the resulting carbon dioxide are ignored; the transfer of heat throughout the process is ignored.

(10) All physical properties are assumed to be immutable.

(11) The contact resistance between layers is ignored.

2.1.2 Electrochemical equation

2.1.2.1 Electrochemical kinetics. The reaction mechanism of the electrooxidation reaction of methanol at the anode and the electroreduction reaction of oxygen at the cathode is relatively complex, and its electrochemical reaction rate can be described by the Butler–Volmer rate expression,[42] which can be simplified to obtain a Tafel type equation of methanol concentration, as shown below.

$$j_a = A \cdot i_{0,a}^{ref} \left(\frac{C_{MeOH}}{C_{MeOH}^{ref}}\right)^{\gamma_a} \exp\left(\frac{6F\alpha_a\eta_a}{RT}\right) \quad (1)$$

$$j_c = A \cdot i_{0,c}^{ref} \left(\frac{C_{O_2}}{C_{O_2}^{ref}}\right)^{\gamma_c} \exp\left(-\frac{6F\alpha_c\eta_c}{RT}\right) \quad (2)$$

where j_a and j_c (A m^{-2}) are the reference exchange current density multiplied by the specific surface area A (1 m^{-1}) of the anode and cathode sides, γ_a and γ_c are the anode and cathode reaction order, η_a and η_c are the anode and cathode activation over (over) potential (V), and α_a and α_c are the anode and cathode transfer coefficients, respectively. C_{MeOH} and C_{O_2} are the concentrations of methyl alcohol and oxygen in the CL (mol m^{-3}). The superscript ref represents the reference concentration.

The overpotential η_a and η_c for the anode and cathode at any location within the CL is defined as follows.

$$\eta_a = \phi_s - \phi_m - E_{eq}^a \quad (3)$$

$$\eta_c = \phi_s - \phi_m - E_{eq}^c \quad (4)$$

where ϕ_s is the potential of the electron-conducting phase of the CL, ϕ_m is the potential of the ionomer phase, and E_{eq} is the thermodynamic equilibrium potential of the cell.

2.1.2.2 Ohm's law. The transport of protons and electrons in the membrane electrode assembly follows Ohm's law. The general equation form can be given by the following formula.

$$\nabla \cdot (-\sigma_m^{eff} \nabla\phi_m) = i_m \quad (5)$$

$$\nabla \cdot (-\sigma_s^{eff} \nabla\phi_s) = i_s \quad (6)$$

where σ_m^{eff} and σ_s^{eff} are the effective conductivity of the ionomer electrolyte and the solid phase, ϕ_m and ϕ_s are the potential of the ionomer electrolyte and the solid phase, and i_m and i_s are the charge source terms of protons and electrons related to electrochemical reactions, respectively.

2.1.3 Governing equation

2.1.3.1 Mass conservation equation. The mass conservation equation (continuity equation) basically requires that the change in mass per unit volume in a given time must be equal to the sum of all substances entering or leaving that volume. The mass conservation equation is

$$\frac{\partial(\varepsilon\rho)}{\partial t} + \nabla \cdot (\varepsilon\rho v) = 0 \quad (7)$$

where ε is the porosity, ρ is the material density, and v is the fluid velocity field. S_{mass} is the mass source term, indicating the rate of mass change per unit volume of each layer of the cell structure. The electrochemical reaction only occurs in the CL; thus, the mass change of the reaction substance only

exists in the catalytic layer, while the other parts of the mass source term are 0 and only exist in the catalytic layer.

$$\frac{\partial(\varepsilon\rho)}{\partial t} = S_{\text{mass}}. \tag{8}$$

2.1.3.2 Charge conservation equation. Momentum transfer can be described by the Navier–Stokes equation.[43] The flow of methanol in the flow channel is considered laminar and continuous, and the momentum of the flow comes from the pressure difference ∇P.

$$\frac{\partial(\varepsilon\rho v)}{\partial t} + \nabla\cdot(\varepsilon\rho vv) = -\varepsilon\nabla P + \nabla\cdot(\varepsilon\mu\nabla v) + S_{\text{v}} \tag{9}$$

Since the steady-state system is used, it will not change with time, and the above formula can be simplified as follows.

$$\nabla\cdot(\varepsilon\rho vv) = -\varepsilon\nabla P + \nabla\cdot(\varepsilon\mu\nabla v) + S_{\text{v}} \tag{10}$$

where ρ is the density of the methanol solution (kg m^{-3}), v represents the flow rate of the liquid (m s^{-1}), P is the liquid pressure (Pa), ε is the porosity, whose value in each part of the cell is different, μ is the liquid viscosity coefficient (kg m^{-1} s^{-1}), and S_{v} is the source term.

2.1.3.3 Species conservation equation. The transport of substances through the anode and cathode is controlled by a combination of diffusion and convection.

$$\rho(u\cdot\nabla)w_i = \rho D_i^{\text{eff}}\nabla^2 w_i + S_i \tag{11}$$

where w_i is the mass fraction of species i and D_i^{eff} is the effective diffusion coefficient. The source term S_i describes the consumption or production (electrochemical and chemical) of species i, and it applies only to the CL. The mass fraction can be calculated from the mole fraction(x_i)

$$w_i = x_i\frac{M_i}{M} \tag{12}$$

where M_i is the molecular weight of substance i and M is the average molecular weight of the mixture.

2.1.3.4 Membrane permeability equation. The transfer of methanol through Nafion membranes occurs through diffusion and electroosmosis. Since the pressure difference between the two sides of the membrane is negligible, methanol permeated from the anode passes through the membrane to the cathode CL and is then completely consumed, resulting in a parasitic current; thus, the methanol permeation equivalent current density (I_{xover}) is determined by the following formula.

$$I_{\text{xover}} = 6FN_{\text{MeOH}}^{\text{M}} \tag{13}$$

The cross flux of methanol is calculated by eqn (2)–(13).

$$N_{\text{MeOH}}^{\text{M}} = -D_{\text{MeOH}}^{\text{M}}\nabla C_{\text{MeOH}}^{\text{M}} + n_{\text{MeOH}}^{\text{EOD}}\frac{I_{\text{cell}}}{F} \tag{14}$$

where $N_{\text{MeOH}}^{\text{M}}$ is the flux of methanol through the membrane, $n_{\text{MeOH}}^{\text{EOD}}$ is the resistance coefficient of methanol electroosmosis, and $D_{\text{MeOH}}^{\text{M}}$ is the diffusion coefficient of methanol in Nafion.

2.1.4 Solver setup. The concentration fractions of methanol (c_{MeOH}) and water ($c_{\text{H}_2\text{Oa}}$) in the anode and the mass fractions of oxygen (w_{O_2}), nitrogen (w_{N_2}) and water ($w_{\text{H}_2\text{Oc}}$) in the cathode are solved in the flow channel, gas diffusion layer (GDL) and CL. The boundary conditions are as follows. (1) Zero flux conditions at the inlet mass fraction or inlet concentration and other external boundaries. (2) Velocity (u) and pressure (P) are solved by Brinkmann equations in the flow channel, GDL, and CL. (3) The inlet velocity and outlet pressure of laminar flow are zero. In addition, symmetry conditions apply to other walls. (4) Ohm's law is used to solve the electron potential (ϕ_{s}) in GDL and CL and the ion potential (ϕ_{m}) in CL and membrane. (5) The local current density depends on the ϕ_{s} and ϕ_{m} in CL and the local reactant concentration. (6) The anode is electrically grounded ϕ_{s} = 0, the cathode ϕ_{s} = E_cell, and the rest of the external boundaries are electrically insulated. Table S1† shows detailed boundary conditions. Due to the nonlinearity of the equations, a stable nonlinear setting is used and a direct solver is used to solve each governing equation in turn.

2.2 Machine learning

In this study, we applied seven different ML algorithms to process the data. In order to improve the fitness of ML model and database, we correctly processed and evaluated the performance of seven model algorithms based on Root Mean Square Error (RMSE). In performance prediction, we chose three algorithms with the smallest RMSE, namely, ETR, RFR and XGB for performance prediction. Two of these methods involve linear regression methods (Lasso, Ridge), and five involve nonlinear regression methods (including two kernel methods (KRR, SVR) and three tree integration methods (RFR, XGB, and ETR)). This set of ML models covers a wide range of model types that can reveal relevant aspects of different data.

The quantitative evaluation of prediction accuracy is based on the root-mean-square error calculated by 10-fold cross-validation, which is the most commonly used method in prediction error estimation.[44–48] Ten-fold cross-validation is an ML cross-validation method that divides the data set into 10 subsets, each of which is used to train the model and then combines the results of these 10 subsets to evaluate the performance of the model. The main advantage of ten-fold cross-validation is that the performance of the model can be evaluated in a shorter period of time as it only needs to evaluate the results of 10 subsets rather than the entire data set. Furthermore, ten-fold cross-validation can also help find potential flaws in the model as it can find problems in the model in a shorter period of time. Herein, we used ten-fold cross-validation to evaluate the predictive performance of the model.

To evaluate the input feature variables that contribute the most to the prediction of the target of interest, the feature importance score provided by the tree-integration method was used.[49,50] The importance score, which can be of many types, is usually calculated as a weighted average of the squared error improvement attributed to a single feature variable and rep-

resents the relative importance of each feature variable relative to the predictability of the target variable. The input feature variables are rarely equally correlated and usually only a few have a significant effect on the predicted target variable.

We then extend this further to predict the entire output *I–V* polarization curve of the DMFC. An SBO (surrogate-based optimization) strategy based on the sequential model-based algorithm configuration (SMAC) program was developed and evaluated using expected improvement (EI). EI calculates the expected improvement value for each candidate configuration based on the prediction results and uncertainty of the current surrogate model. This value typically considers two factors: the performance prediction (mean) and the uncertainty (standard deviation) of the candidate configuration. By comparing the EI values of different candidate configurations, the SBO strategy can select the most promising one.

All of the ML computational work was done by writing code in the Python 3.7 environment. All ML models make extensive use of the Scikit-learn package (version 0.24.1) and XGB uses the XGBoost package (version 1.3.3).

3. Results and discussion

3.1 Grid independence verification

In this study, COMSOL Multiphysics was used as the finite element solver. In order to simplify the model and improve the computing efficiency, we cut out a part of the structure of the DMFC and constructed a model including the flow channel of the positive (negative) electrode, the diffusion layer of the positive/negative electrode, the catalytic layer of the positive/negative electrode, and the proton exchange membrane. After entering all the necessary equations (secondary current distribution, transport of dilute matter, transport of dense matter, Brinkman equations, phase transport of porous media and electrochemical relations), a grid was generated for the geometry using the software's built-in module. Fig. 1 shows the DMFC model after grid division. The structured hexahedral grid was generated by scanning and mapping methods. To build the grid, the maximum cell size was set to 1 mm and the maximum element growth rate was set to 1.5. Grid independence verification can determine the balance between calculation speed and calculation accuracy.[51–53] Fig. S1† shows the results of the grid independence verification. Considering the cost and time, the number of mesh encryption layers is selected as the norm after balancing the accuracy and calculation.

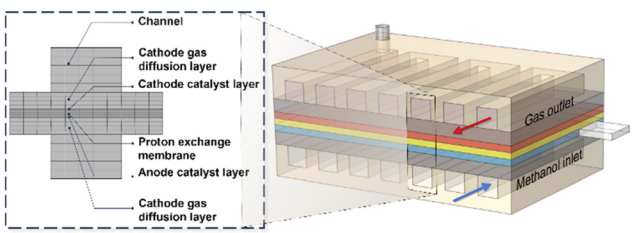

Fig. 1 3D geometric model of DMFC.

3.2 DMFC simulation model

The geometric parameters, physical and chemical properties and operating conditions used in this modeling work are shown in Table S2.† The operating temperature was maintained at 333.15 K, the methanol concentration was 1 M, and the flow rates of methanol and air were 6 mL min^{-1} and 600 sccm, respectively. More details corresponding to the literature simulation can be found in the references.[54] It can be seen from Fig. 2(a) that the simulated polarization curve is consistent with the simulation results in the literature. The polarization curve of the simulated 1 M methanol solution was compared with the calculated polarization curve obtained from the experimental data obtained in the research group's literature,[55] as shown in Fig. 2(b). In the experiment, the materials used in the fuel cell included Nafion 115 for the membrane and Pt–Ru with a loading of 0.2 mg cm^{-2} for the anode CL. Methanol solution and air flow were supplied to the anode and cathode at 80 °C, respectively. Anode inlet flow rate Q_a was set at 2 mL min^{-1}, and cathode inlet flow rate Q_c was set at 100 sccm. The simulation results are in good agreement with the experimental values of the research group, which proves that the three-dimensional multi-phase model is accurate, reliable and reasonable.

For a cell voltage of 0.25 V (voltage at maximum power density), the distribution of methanol concentration, CO_2 concentration, oxygen concentration and cathode water concentration is shown in Fig. S2.† From the distribution of substance concentrations in the figure, it can be seen that fluid flow has been fully developed in the channel. In Fig. S2(a–d),† methanol concentration decreases along the length direction (*y* positive direction) and thickness direction (*z* positive direction) as methanol is transmitted through the flow channel to CL, and methanol just participates in the reaction at the entrance; thus, less methanol is consumed and the current density is lower. With the diffusion of methanol, the more intense the reaction, the greater the reduction of methanol concentration. Methanol concentration ranges from 1000 to 997.75 mol m^{-3}. As a product, the concentration distribution of CO_2 is completely opposite to that of methanol, increasing from 0.0001 to

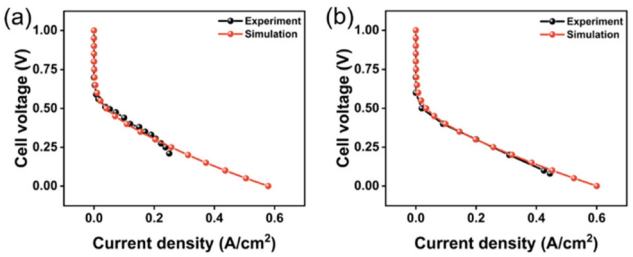

Fig. 2 (a) Comparison of polarization curve with polarization curve obtained from simulation literature parameters[54] and (b) Comparison of polarization curve with polarization curve obtained from experimental literature parameters.[55]

2.2485 mol m^{-3}. This suggests that the more the methanol diffuses, the more intense the reaction in the middle. The concentration distribution of oxygen and water corresponds to the concentration distribution of methanol and CO_2, respectively. Oxygen and protons in the cathode CL generate water, oxygen consumption, and liquid water. The distribution of water is mainly concentrated in the cathode CL and GDL, which makes it easy to accumulate water, and the phenomenon of "water-flooding" occurs.[56] The methanol permeated from the anode reaches the cathode CL, where it is then completely consumed, and the resulting current indicates the amount of methanol permeated. The unreacted methanol is transported to the cathode by diffusion and electroosmosis driving forces. In Fig. S2(e),† it can be seen that the methanol flux per unit time in the cathode CL is very low, indicating a very low cross-current density. The saturation distribution of the cathode liquid is shown in Fig. S2(f).† There is a clear dividing line between the flow channel and the cathode GDL interface. However, the amount of change is small because the change in the saturation of liquid water in the cathode can be considered negligible.

3.3 The polarization curve obtained by CL key parameter screening

The polarization curve serves as a tool to describe the performance and performance losses of fuel cells under various operating conditions. The polarization curve can be divided into three regions: activation polarization, ohmic polarization, and mass transport polarization. Among them, activation polarization is caused by the slow reaction on the electrode surface. Ohmic voltage drop arises from the resistance to ion transport in the anode, cathode, electrolyte, and other interconnections. Mass transport polarization results from the existence of certain resistance in the mutual transport of fuel and oxygen during electrode reactions. By optimizing the parameters to improve these three polarization regions, the performance of fuel cells can be enhanced.

Therefore, we selected temperature, anode/cathode CLs thickness, porosity, Nafion content, anode inlet flow rate, cathode inlet flow rate, anode catalytic layer permeability, cathode catalytic layer permeability, anode methanol inlet concentration, anode specific surface area, cathode specific surface area, reference pressure, anode/cathode electron conductivity, anode/cathode proton conductivity, reference methanol concentration, reference oxygen concentration, a total of 19 parameters that may affect the polarization phenomenon, as input characteristics. For each parameter, we tried to choose the one with the lowest correlation. The power density is considered to be the output.[57,58] Table 1 lists the input parameters and their value ranges. Then, we built a database of fuel cells.

3.3.1 Active specific surface area. Electrochemistry has become an important topic in nanomaterials because of its applications in energy storage and conversion. A particularly important parameter for the electrochemical applications of nanomaterials is electrochemically active specific surface area (ECSA). Therefore, the accurate estimation of ECSA is very important for the determination of catalyst performance. The electrochemical kinetics equation is related to the active specific surface area (Av) (1 m^{-1}) on the anode and cathode sides. Av refers to the active area of the electrode–electrolyte interface that is catalytically active for the catalytic layer reaction. The relationship between Av and ECSA is as follows.

$$\mathrm{Av} = \frac{\mathrm{ECSA}}{\nu_{\mathrm{pt}}} \tag{15}$$

Therefore, the ECSA can be changed by controlling the Av when the Pt loading volume is unchanged.

Fig. 3 shows Av changes for different anode and cathode CLs. As can be seen from the polarization curve in Fig. 3(a), anode Av can cause large ohmic polarization and concentration polarization but has little effect on activation polarization. The cell performance increases as the Av range increases

Table 1 Input variables and corresponding variable ranges

Variables	Expression	Range
Temperature (K)	T (K)	288.15–378.15
Thickness of anode CL (m)	H_electrode_an (m)	(5×10^{-7})–(7.5×10^{-5})
Thickness of cathode CL (m)	H_electrode_ca (m)	(5×10^{-7})–(7.5×10^{-5})
Porosity of anode CL (%)	eps_CL_p_a (%)	10–90
Porosity of cathode CL (%)	eps_CL_p_c (%)	10–90
Nafion content of anode CL (%)	eps_CL_l_a (%)	5–60
Nafion content of cathode CL (%)	eps_CL_l_c (%)	5–60
Anode inlet flow rate (m s^{-1})	U_in_an (m s^{-1})	0.01–2
Cathode inlet flow rate (m s^{-1})	U_in_ca (m s^{-1})	0.1–8
Permeability of anode CL (m^2)	kappa_CL_an (m^2)	(1×10^{-15})–(5×10^{-11})
Permeability of cathode CL (m^2)	kappa_CL_ca (m^2)	(1×10^{-15})–(5×10^{-11})
Anode methanol inlet concentration (M)	C_{MeOH}_in (M)	0.1–15
Anode specific surface area (1 m^{-1})	Av_an (1 m^{-1})	(1×10^{4})–(1×10^{7})
Cathode specific surface area (1 m^{-1})	Av_ca (1 m^{-1})	(1×10^{4})–(1×10^{7})
Reference pressure (atm)	p_ref (atm)	0.1–8
Positive cathode electron conductivity (S m^{-1})	sigma_CL_s (S m^{-1})	10–1000
Positive cathode proton conductivity (S m^{-1})	sigma_CL_i (S m^{-1})	1–19
Reference methanol concentration (mol m^{-3})	c_{MeOH}_ref (mol m^{-3})	10–500
Reference oxygen concentration (mol m^{-3})	$c_{\mathrm{O_2}}$_ref (mol m^{-3})	5–50

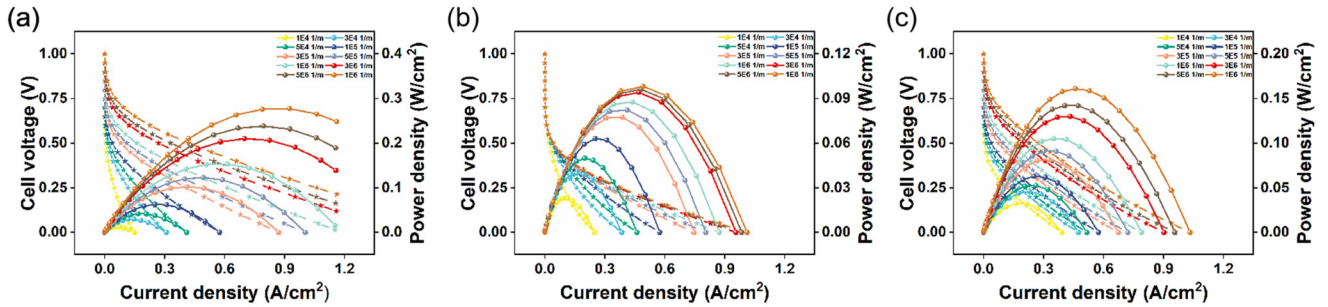

Fig. 3 Polarization curve obtained by changing the active specific surface area (Av): (a) anode CL; (b) cathode CL; (c) the anode and cathode CLs.

from 1×10^4 to 1×10^7, and the increase trend is more gradual at 3×10^5. The final Av is 2.3 times larger than the previous one, while the maximum power density is only 16% better. It may be due to the failure of the reaction products to leave the catalyst surface, which leads to the mass transfer obstruction, thus limiting the performance improvement. As can be seen from the polarization curve in Fig. 3(b), the change in Av has a great influence on activation polarization and ohmic polarization. As the current density increases, the impact of Av on cell performance gradually increases. More and more active sites on the cathode are involved in the reaction, which is conducive to the oxygen reduction reaction. In Fig. 3(c), when the Av of the anode and cathode CLs is changed at the same time, the cell performance improvement is not obvious when the anode Av or cathode Av is increased separately because the anode Av and cathode Av are increased at the same time; thus, the reaction products of the cathode and anode cannot be transmitted out in time, which affects the cell performance. Therefore, when optimizing the electrochemical system, it is necessary to comprehensively consider the synergistic effect of the anode and cathode to ensure the effective transmission of reaction products to achieve the best performance.

3.3.2 Anode and cathode CLs thickness. The thickness of the catalytic layer is a parameter closely related to the activation polarization, ohmic polarization and concentration polarization of the cell. It not only affects the species and charge transfer inside the catalytic layer but also affects the size of the catalytic active area inside the catalytic layer.[59,60] The thickness of anode CL and cathode CL is included in this model. Fig. 4 shows the current density and power density polarization curves of catalytic layers with thicknesses of 500 nm, 1 μm, 5 μm, 15 μm, 25 μm, 35 μm, 45 μm, 55 μm, 65 μm and 75 μm. It can be seen from Fig. 4 that the performance of DMFC increases with the increase in CL thickness because the increase in the thickness of the catalytic layer is accompanied by an increase in the catalytic active area. When the thickness is greater than 25 μm, the performance improvement of the cell slows down. As the thickness of the catalytic layer increases, the mass transfer path increases and the mass transfer resistance increases. In addition, the thick catalytic layer may also cause an increase in the internal resistance, which further affects the cell performance. Therefore, for the selection of catalytic layer thickness, on the one hand, it is necessary to ensure that the catalytic layer is thick enough to provide enough catalytic active area. On the other hand, it is necessary to avoid the increase in mass transfer resistance and internal resistance caused by excessive thickness.

3.3.3 The ratio between porosity and Nafion in the CL. Pores are conducive to the transport of substances, and Nafion is conducive to the transport of protons. Fig. S3† shows the polarization curves of the CL at different porosities and Nafion ratio. Fig. S3(a)† shows the effect of porosity on the performance of the cell while the Nafion content remains unchanged. In this model, the volume of the catalytic layer is fixed; thus, the increase in the porosity is accompanied by the decrease in the volume of the catalyst. On one hand, the presence of pores

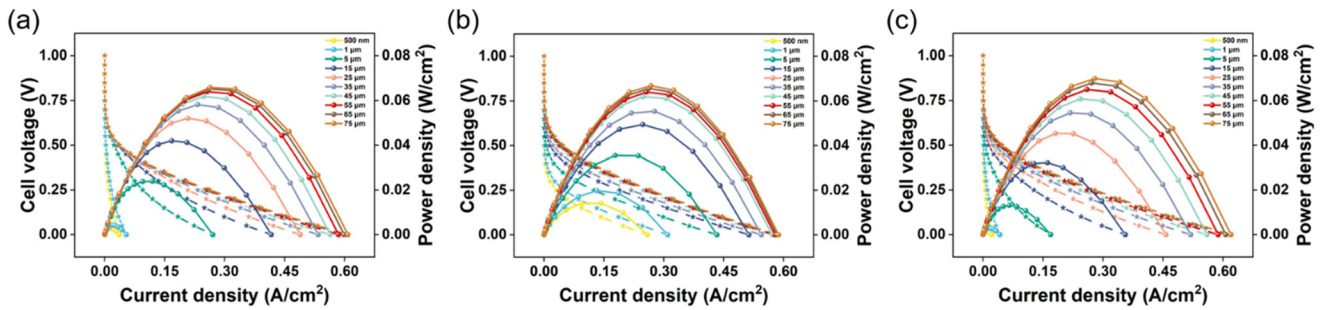

Fig. 4 Polarization curve obtained by changing the CL thickness: (a) change of anode CL thickness; (b) change of cathode CL thickness; (c) change of anode and cathode CLs thickness.

provides a channel for the diffusion of gases as well as the release of water, which is essential for reaction kinetics. On the other hand, the decrease in the catalyst content also reduces the performance of the cell, so there is little change in Fig. S3(a). Fig. S3(b)† shows that the catalyst content remains unchanged, while the porosity and Nafion content change. It can be found that the performance of the cell increases with the increase in the proportion of Nafion content. When the ratio of Nafion exceeds 0.25, the improvement of cell performance slows down. This is because Nafion will promote the conduction of ions, but when the content of Nafion is too high, it will lead to the reduction of the porosity of the catalytic layer and thus hinder the gas conduction. Fig. S3(c)† shows the polarization curve when the porosity is unchanged and the catalyst changes at the same time. It can be seen that when the porosity is consistent, the larger the proportion of Nafion, the larger the cell power density. When the Nafion ratio is unchanged, the increase in porosity has almost the same effect on the performance of the cell. In summary, the effect of Nafion ratio in CL is greater than that of porosity, and proton transport may play a more important role than species transport.

3.3.4 Inlet velocity of methanol at the anode and oxygen at the cathode. When DMFC is running, the methanol solution and oxygen are constantly transferred from outside the cell to inside the cell, and the substances inside the cell are constantly consumed by electrochemical reactions. In general, the more rapid the replenishment of the external substances, the smaller the difference between the actual concentration and the supplied reactant concentration. Thus, the magnitude of the reactant concentration is not only related to the concentration provided but also to the flow rate of the substance. As can be seen from Fig. S4(a),† changes in the inlet velocity of the anode methanol solution in the range of 0.01 m s^{-1} to 2 m s^{-1} have little impact on the performance of the cell. This may be because within this flow rate range, the transmission speed of methanol is already fast enough to meet the requirements of the internal electrochemical reactions of the fuel cell, or there may be other factors (such as methanol permeation and proton exchange membrane performance) that limit the improvement of the fuel cell performance, making the impact of flow rate changes on performance less obvious. As can be seen from Fig. S4(b)†, the cell performance increases with the increase in the cathode intake flow. When the flow rate increases to a certain range, the cell performance gradually improves. When the cathode air flow rate increases from 0.1 m s^{-1} to 0.5 m s^{-1}, the cell performance is improved with the increase in the cathode air flow rate, and the performance is greatly improved. When the cathode air flow rate increased from 0.5 m s^{-1} to 8 m s^{-1}, the output performance of the cell did not change, the polarization curve did not change at low current density, and the cell performance was slightly improved at medium and high current density. When the consumed reactants are replenished in time, the increase in the cathode air flow rate reduces the concentration polarization loss of the cell. In real fuel cell operation, excessively high methanol and oxygen flow rates may also result in additional pump power losses, reducing the overall efficiency of the fuel cell system.

3.3.5 Temperature and pressure. Temperature and pressure are two important factors that affect the performance of fuel cells. It can be found from Fig. S5(a)† that in the region with low current density, the power density in the temperature range of 15–55 °C is basically the same. Within this temperature range, the electrochemical reaction rate and substance diffusion rate inside the fuel cell remain relatively stable without significant changes. When the temperature is located in the range of 55–85 °C, in the region with high current density, higher the temperature, higher the power density. Because when the temperature increases, the electrochemical reaction activity will increase. In addition, the diffusion rate of methanol and oxygen will also increase, helping to enhance the electrochemical reaction of the anode and cathode. On continuously raising the temperature, and the cell's performance will deteriorate. High temperature will lead to a large amount of methanol and water vapor loss, thereby reducing the efficiency of the cell. In the real operation of the cell, high temperature will reduce the performance of the proton exchange membrane and may also lead to catalyst deactivation. Therefore, in practical operation, it is necessary to find an optimal operating temperature range to ensure that the fuel cell operates in an efficient and stable state.

Fig. S5(b)† shows the polarization curve under different working pressures from 0.1 to 8 atm. In the small current range, the effect of increasing pressure on the output performance of the fuel cell is not significant, while in the large current range, the effect of increasing pressure on the output performance is gradually improved. The higher the pressure, the better the output performance of the fuel cell system. However, the specific working pressure that can be achieved depends on the maximum pressure that the stack and the membrane electrode can withstand. In addition, in real situations, high pressure can lead to an increase in the parasitic power of related equipment, which can offset some of the performance improvements caused by increased pressure, thereby reducing the net power density of fuel cells. When designing and optimizing fuel cell systems, it is necessary to comprehensively consider factors such as performance under different pressures, system complexity, and cost to achieve optimal power density and performance.

3.3.6 Electron conductivity and proton conductivity. Charge consists mainly of two kinds of charged particles, namely, electrons and ions. Therefore, there are two kinds of losses in the charge transfer process of proton-exchange membrane fuel cells, namely, the loss of electrons passing through solid phase conductors such as catalytic layer and diffusion layer and the loss of protons passing through the proton exchange membrane. According to charge transport loss, conductivity can be divided into solid phase conductivity (electronic conductivity) and membrane phase conductivity (ionic conductivity).

Fig. S6(a)† shows the polarization curves for different electron conductivities of the positive cathode catalytic layer. In order to ensure that the catalytic layer and the diffusion layer have good electrical conductivity and ensure electron transmission, the electronic conductivity needs to be hundreds or more. In this paper, the cell performance is calculated in the range of 10–1000 S m^{-1}, and it is found that the change in the electronic conductivity has little effect on the cell performance. This is because the electronic conduction path has been effectively established at the three-phase interface. However, this does not mean that electronic conductivity can be completely ignored. In practical applications, if the electronic conductivity is insufficient, it may lead to an increase in internal resistance of the fuel cell, thereby affecting the output performance and efficiency of the fuel cell.

Generally speaking, the conductivity of the membrane is below 20 S m^{-1}, and the main range of the effective proton conductivity discussed here is 1–19 S m^{-1}. The proton conductivity is closely related to the water content of the Nafion membrane, which is related to the proton transport process and mode. The conductivity of the proton-exchange membrane plays an important role in charge transport loss. As shown in Fig. S6(b),† in the low current density region, the efficiency of the fuel cell is mainly affected by activation loss; thus, it is insensitive to effective proton conductivity and does not show significant changes. At medium to high current densities, Ohmic loss becomes the main component of fuel cell performance loss. The improvement of proton conductivity helps to reduce Ohmic losses. However, as proton conductivity increases, the rate of improvement in fuel cell performance will gradually slow down, and there may even be a convergence trend. This is because when the proton conductivity reaches a certain level, the efficiency of proton transport in the membrane is close to its limit, and a further improvement of proton conductivity will have limited impact on the fuel cell performance.

3.3.7 Anode reference concentration of methanol and cathode reference concentration of oxygen. In the Butler–Volmer equation, the exchange current density (i_0) is a key parameter that reflects the rate of electrochemical reaction at equilibrium potential. According to this equation, the exchange current density is inversely proportional to the reference concentration of the reactants. This means that when the reference concentrations of methanol and oxygen are low, the exchange current density will be relatively high. As shown in Fig. S7,† the calculated results also show the same conclusion.

This conclusion can be explained from the perspective of electrochemical kinetics. A smaller reference concentration means that the concentration gradient of reactants on the electrode surface is larger, thereby promoting the diffusion of reactants and increasing the reaction rate. Therefore, in fuel cells, optimizing the supply and concentration distribution of methanol and oxygen can potentially improve the exchange current density, thereby enhancing the performance of the cell.

3.3.8 Anode methanol inlet concentration. For DMFC, if only DMFC specific power is considered, the higher the methanol concentration, the more favorable it is for the cell. However, at this stage, due to the material properties, the proton-exchange membrane of DMFC has the problem of methanol penetration, and its concentration directly affects the degree of DMFC's penetration of methanol.[61] The reasonable choice of methanol concentration is very important for DMFC performance. This paper calculates the range of methanol concentration from 0.1 M to 15 M. As shown in Fig. S8,† with the increase in methanol concentration, the performance of the fuel cell also improves but the degree of improvement gradually decreases with the increase in concentration. Especially below 3 M, the performance improvement of fuel cells is particularly significant, and the concentration polarization effect is obvious. When the concentration exceeds 3 M, the trend of changes in fuel cell performance tends to flatten out, and the impact of concentration polarization on fuel cell performance gradually decreases.

Finally, we organized the amplitude range of the maximum power density of the direct methanol fuel cell simulation model after adjusting each parameter to understand the importance of each parameter on the maximum power density. The results are shown in Fig. S9,† which displays the top six parameters in terms of maximum power density amplitude ranking.

3.4 Model- and data hybrid-driven prediction

3.4.1 Database establishment. In order to collect the training data, the ML model needs to be trained. A database is built based on the data obtained from different ranges affecting the different parameters of CL. CL different parameters are used as input features and power density is considered as the output. Table S3† lists the input elements and the corresponding ranges of values.

3.4.2 Evaluation of different ML models. Seven algorithms have been adopted to make predictions on the given input features. To quantify accuracy, the training test segmentation was retained. The predictions for the test set are plotted in Fig. 5 and Fig. S10.† The x-coordinate represents the predicted power density, while the y coordinate represents the actual value of the power density. Therefore, the closer the data point is to the slash line "$y = x$", the closer the predicted value is to the actual value.

We chose root mean square error (RMSE) and standard deviation (STD) to evaluate the prediction accuracy of the algorithm. Table 2 shows the RMSE and STD of the data training test obtained by seven different algorithms. Nonlinear

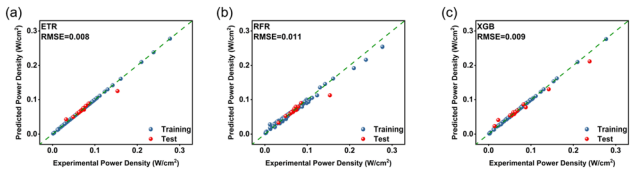

Fig. 5 Data training test (10-fold cross-validation) error graph of three algorithms based on the tree-integration method. (a) ETR; (b) RFR; (c) XGB. Training data (blue), test data (red).

Table 2 Training and testing root mean square error of data obtained from 7 different algorithms

Method	Lasso	Ridge	KRR	ETR	RFR	SVR	XGB
RMSE_test (STD_test)	0.024	0.024	0.044	0.008	0.011	0.028	0.009
	0.009	0.009	0.016	0.003	0.004	0.011	0.003
RMSE_train (STD_test)	0.019	0.017	0.025	0.003	0.005	0.013	0.003
	0.001	0.001	0.001	0	0	0.001	0

methods (KRR, SVR, RFR, XGB, ETR) perform better than linear methods (Lasso, Ridge), and in particular, tree-integration methods (RFR, XGB, and ETR) have smaller training and test errors because they can capture nonlinear relationships in data, have better robustness and generalization ability, automatically evaluate feature importance and adapt to different types of data distributions and feature sizes, and have high computational efficiency and good scalability. It is worth mentioning that the ETR algorithm has excellent performance in the RMSE (0) and STD (0) evaluation criteria and has advantages such as strong anti-overfitting ability, high computational efficiency, and insensitivity to outliers. Therefore, we decide to use ETR algorithm to predict the optimal parameter combination. As for the computation time, simulation models typically require tens of seconds to minutes, while surrogate models typically only require a few seconds. This will greatly improve the computational efficiency of the model, making real-time interaction of key information between physical and simulation models possible in digital twin systems. The surrogate model based on ETR has better application prospects in the state-monitoring system of direct methanol fuel cells.

3.4.3 Feature importance ranking. The influence of CL parameters on the power density in DMFC was evaluated, and the input variables that most contributed were predicted. For this purpose, the feature importance score is calculated from the RFR, XGB, and ETR models optimized by the proposed ML method. The feature importance score is a measure used to assess the importance of features in a data set. It is calculated by taking the average of the importance of each feature and dividing by the total number of features. The higher the feature importance score, the more important the feature is in the data set. Feature importance score evaluates each hyperparameter, and the results are shown in Fig. 6. The larger the feature importance score, the better the distinguishing ability of the corresponding features. Therefore, the first three important characteristics recognized by all the three algorithms are the specific surface area of the cathode, the specific surface area of the anode, and the thickness of the anode. The parameters with the highest importance in terms of their features are highly consistent with the parameters that have the greatest impact on the maximum power density amplitude of the model, as previously determined. We can view this result as intelligent confirmation that RFR, XGB, and ETR are indeed capable of recognizing various parameters. It is worth noting that under high voltage conditions, fuel cells will generate parasitic power during actual operation, thereby reducing the net power density of the fuel cell. In order to consider the impact of high pressure on the power density as much as possible, we calculated the ratio of maximum power density to different pressures and used the obtained data to reorder the importance of parameters. As shown in Fig. S11,† the ranking changes of different average feature importance are very small compared to the data without considering the influence of pressure. This, to some extent, indicates that it is acceptable to temporarily disregard the impact of pressure on the results.

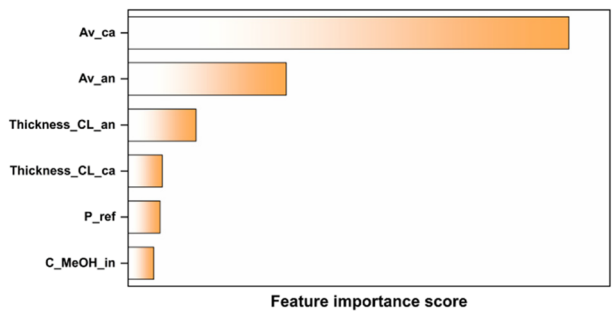

Fig. 6 Average feature importance prediction plots based on the best ETR models in ten-fold cross-validation (top 6).

3.4.4 Polarization curve prediction. The EI score is a measure used to evaluate the performance improvement of an ML model over time.[62–64] It is calculated by taking the average of the model accuracy improvement over time and dividing it by the total number of iterations. Over time, the higher the EI score, the better the performance of the model. In this study, SMAC and EI score were used for evaluation. Fig. 7 shows the top ten parameter combinations sorted by EI score. The top three parameter values for feature importance are shown on the left side of the figure.

In order to test the learning results of SMAC, we brought the 10 groups of parameters with the highest expected improvement value into the model and performed numerical

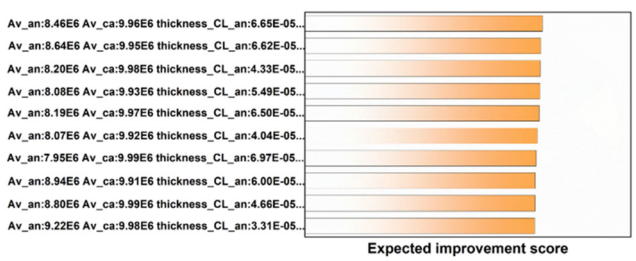

Fig. 7 The EI score of the top 10 combinations obtained through ML.

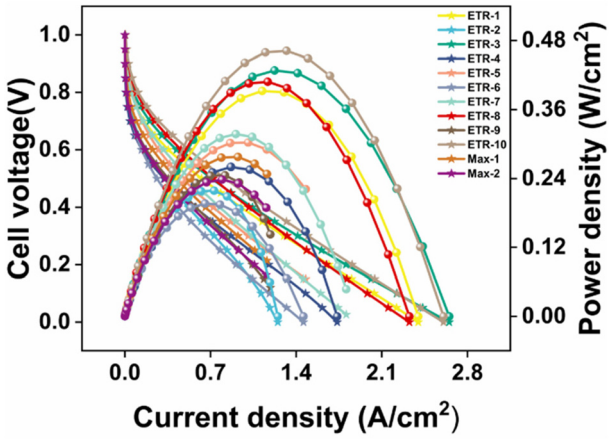

Fig. 8 Comparison between the top 10 EI score data and the polarization curve of the original database.

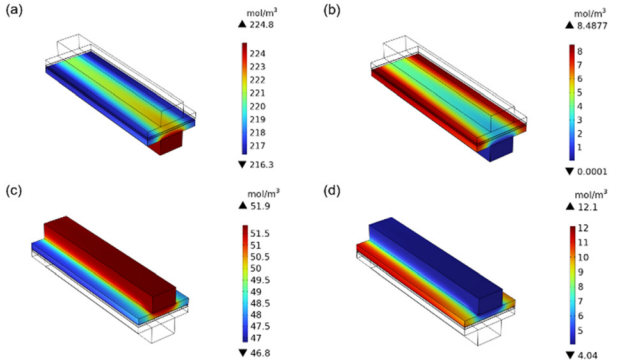

Fig. 9 The concentration distribution of reactants and products (0.35 V) was predicted by the optimal parameter combination: (a) molar concentration of methanol at the anode, (b) molar concentration of CO_2 at the anode, (c) molar concentration of oxygen at the cathode, and (d) molar concentration of water at the cathode.

simulation to obtain their *I–V* polarization curves and compared them with the polarization curves of the first and second power density in the original database. As shown in Fig. 8, compared with the original database, more than half of the polarization curves obtained by the top 10 parameter combinations with the EI score exceeded the maximum power density of the original database.

The model we have established has the ability to capture dynamic effects. As shown in the ESI Movie S1,† it illustrates the concentration change process of methanol in the cathode of a methanol fuel cell. It can be seen that methanol diffuses in the flow field and reacts with GDL after coming into contact with the catalytic layer. The concentration of methanol decreases sequentially from the fuel inlet to the outlet, from the middle to both sides. To explore the internal mechanism of the performance improvement, we selected the optimal parameter combination to analyse the distribution of the reactants and products. Compared with the initial parameters, the thickness of the cathode catalytic layer, the flow rate of the channel, the permeability and the specific surface area of the cathode and anode all increase.[65,66] Compared with the initial parameters, the thickness of the cathode catalytic layer, the channel flow rate of the cathode anode, the permeability and specific surface area of the catalytic layer, as well as the temperature and pressure of the anode catalytic layer all increased, while the thickness of the anode catalytic layer decreased, as shown in Fig. 9. Due to the increase in the anode inlet velocity and the increase in permeability, the distribution of methanol concentration was more uniform than that in the initial model (Fig. S1†). When the cell voltage is 0.35 V (maximum power density voltage), the methanol concentration drops from 224.8 mol m^{-3} to 216.3 mol m^{-3}, which is greater than 2.1 mol m^{-3} of the initial model. The effect of height and high pressure, as well as the increase in the specific surface area of the anode, make methanol oxidation more thorough.[67] The thinner anode catalytic layer also helps reduce methanol penetration. The distribution of CO_2 is completely opposite to that of methanol, which also proves that the methanol reaction is sufficient. The same explanation applies to oxygen and water concentrations. The above conclusions show that the parameter combinations recommended by ML can significantly improve methanol fuel cells, and the ideas provided in this paper also provide new insights into the optimization direction of DMFC.

4 Conclusions

In this study, we combined numerical simulation and ML high throughput to reveal the effects of different parameters of CL on the DMFC performance. First, the optimized models were obtained by training 7 ML algorithms on the database. Then, a comprehensive tree-based regression model (XGB, ETR, and RFR) was used to rank the importance of the 19 complex eigenvalues, and the input eigenvariables with the greatest influence were quantitatively determined. The results of these three algorithms all show the same first three important characteristic values: cathode specific surface area, anode specific surface area and anode thickness. Then, SMAC was used to get the expected improved values of different parameter combinations. The top ten parameter combinations with EI score were selected and imported into the simulation model for testing, and the entire output *I–V* polarization curve of the DMFC was obtained and compared with the *I–V* polarization curve of the maximum power density in the original database. The results show that a majority of the polarization curves obtained from the top combinations exceed the maximum power density of the original database.

We provide a method that leverages simulation models to rapidly establish databases and integrates machine learning to accelerate parameter optimization. However, to reduce computational complexity and enhance simulation efficiency, we simplified the fuel cell system to a certain extent. Real fuel cell operating conditions are influenced by factors across multiple scales, including the microscale (such as electrode material structure, and catalyst layer activity), mesoscale (such as flow channel

design and gas diffusion layer structure), and macroscale (such as overall cell structure and thermal management design). Yet, overly complex models can incur significant computational costs. Additionally, there is often a contradiction between the real-time performance and accuracy of models. To improve the real-time performance, models may need to be simplified or their precision reduced, whereas to enhance accuracy, model complexity and computational load need to be increased. Currently, the concept of digital twins is rapidly gaining popularity, aiming to create virtual replicas of physical entities for data interaction with the actual objects and utilizing machine learning to train data-driven surrogate models based on datasets. The developed surrogate models are expected to offer accuracy comparable to multi-physics predictive physical models while possessing response speeds much faster than those of simulation models. Currently, digital twins have been widely applied in complex systems of various scales, including cities, factories, and airplanes.[68–70] This technology, characterized by high interactivity and rapid optimization iteration,[71,72] can address the aforementioned issues. This work lays the foundation for the establishment of a digital twin model for direct methanol fuel cells. In the future, by training surrogate models, rapid interaction between fuel cell entities and digital models can be achieved, effectively determining and monitoring their multi-physics field states. This has significant implications for fuel cell design and control operations.

Author contributions

Lishou Ban: methodology, formal analysis, writing – original draft. Danyang Huang: conceptualization, data curation. Yanyi Liu: investigation, validation. Pengcheng Liu: software, writing – review & editing. Xihui Bian and Yifan Liu: supervision, resources. Kaili Wang: supervision, writing – review & editing. Xijun Liu: supervision, resources. Jia He: conceptualization, project administration, funding acquisition.

Data availability

The authors will supply the relevant data in response to reasonable requests.

Conflicts of interest

The authors declare that they have no known competing financial interests or personal relationships that could have appeared to influence the work reported in this paper.

Acknowledgements

This work was financially supported by the National Natural Science Foundation of China (52073214) and the Shenzhen Science and Technology Program (JCYJ20230807112503008). This research was supported by TianHe Qingsuo Open Research Fund of TSYS in 2022 & NSCC-TJ.

References

1 Y. J. Wang, J. Qiao, R. Baker and J. Zhang, *Chem. Soc. Rev.*, 2013, **42**, 5768.
2 M. M. Mohideen, A. V. Radhamani, S. Ramakrishna, Y. Wei and Y. Liu, *J. Energy Chem.*, 2022, **69**, 466.
3 J. Zhou, H. Xiao, W. Weng, D. Gu and W. Xiao, *J. Energy, Chem.*, 2020, **50**, 280.
4 W. R. W. Daud, R. E. Rosli, E. H. Majlan, S. A. A. Hamid, R. Mohamed and T. Husaini, *Renewable Energy*, 2017, **113**, 620.
5 Z. Shangguan, B. Li, P. Ming and C. Zhang, *J. Mater. Chem.*, 2021, **9**, 15111.
6 Y. H. Shen, H. Lv, Y. Q. Hu, J. W. Li, H. Lan and C. M. Zhang, *Renewable Energy*, 2023, **212**, 834.
7 H. Mistry, A. S. Varela, S. Kuhl, P. Strasser and B. R. Cuenya, *Nat. Rev. Mater.*, 2016, **1**, 16009.
8 L. Fu, W. Ji, J. He, C. Huang, Y. Li and Y. Dou, *China Powder Sci. Technol.*, 2024, **30**, 170.
9 F. Lyu, M. Cao, A. Mahsud and Q. Zhang, *J. Mater. Chem.*, 2020, **8**, 15445.
10 E. P. Murray, T. Tsai and S. A. Barnett, *Nature*, 1999, **400**, 649.
11 J. Zhao, H. Y. Liu and X. G. Li, *Electrochem. Energy Rev.*, 2023, **6**, 13.
12 P. C. Sui, X. Zhu and N. Djilali, *Electrochem. Energy Rev.*, 2019, **2**, 428.
13 S. Q. Song, W. J. Zhou, W. Z. Li, G. Sun, Q. Xin, S. Kontou and P. Tsiakaras, *Ionics*, 2004, **10**, 458–462.
14 S. Arisetty, C. A. Jacob, A. K. Prasad and S. G. Advani, *J. Power Sources*, 2009, **187**, 415.
15 S. H. Seo and C. S. Lee, *Appl. Energy*, 2010, **87**, 2597.
16 S. H. Yang, C. Y. Chen and W. J. Wang, *J. Power Sources*, 2010, **195**, 2319.
17 S. Chen, F. Ye and W. Lin, *Int. J. Hydrogen Energy*, 2010, **35**, 8225.
18 I. Taymaz, F. Akgun and M. Benli, *Energy*, 2011, **36**, 1155.
19 A. Jason, J. A. Varnell, J. S. Sotiropoulos, T. M. Brown, K. Subedi, R. T. Haasch, C. E. Schulz and A. A. Gewirth, *ACS Energy Lett.*, 2018, **3**, 823.
20 F. Jaouen, M. Lefèvre, J. P. Dodelet and M. Cai, *J. Phys. Chem. B*, 2006, **110**, 5553.
21 N. D. Leonard, K. Artyushkova, B. Halevi, A. Serov, P. Atanassov and S. C. Barton, *J. Electrochem. Soc.*, 2015, **162**, F1253.
22 J. C. Park, S. H. Park, M. W. Chung, C. H. Choi, B. K. Kho and S. I. Woo, *J. Power Sources*, 2015, **286**, 166.
23 Y. Yin, J. Liu, Y. F. Chang, Y. Z. Zhu, X. Xue, Y. Z. Qin, J. F. Zhang, K. Jiao, Q. Du and M. D. Guiver, *Electrochim. Acta*, 2019, **296**, 450.
24 Q. Yang, A. Kianimanesh, T. Freiheit, S. S. Park and D. Xue, *J. Power Sources*, 2011, **196**, 10640.

25 B. Yu, Q. Yang, A. Kianimanesh, T. Freiheit, S. S. Park, H. Zhao and D. Xue, *Int. J. Hydrogen Energy*, 2013, **38**, 9873.
26 M. Tafaoli-Masoule, A. Bahrami and E. M. Elsayed, *Energy*, 2014, **70**, 643.
27 J. Lee, S. Lee, D. Han, G. Gwak and H. Ju, *Int. J. Hydrogen Energy*, 2017, **42**, 1736.
28 J. Jiang, Y. Li, J. Liang, W. Yang and X. Li, *Appl. Energy*, 2019, **252**, 113431.
29 M. S. Hossain and G. Muhammd, *Inf. Fusion*, 2019, **49**, 69.
30 C. Shan, S. Gong and P. W. Mcowan, *Image Vis. Comput.*, 2009, **27**, 803.
31 J. Cao, T. Chen and J. Fan, *Multimed. Tools Appl.*, 2016, **75**, 2839.
32 W. Lou, A. Ali and P. K. Shen, *Nano Res.*, 2022, **15**, 18–37.
33 W. Lei, M. Li, L. He, X. Meng, Z. Mu, Y. Yu, F. M. Ross and W. W. Yang, *Nano Res.*, 2020, **13**, 638.
34 J. Ruan, Y. Chen, G. Zhao, P. Li, B. Zhang, Y. Jiang, T. Y. Ma, H. G. Pan, S. X. Dou and W. P. Sun, *Small*, 2022, 2107067.
35 H. Li, Y. Pan, D. Zhang, Y. Han, Z. Wang, Y. Qin, S. Y. Lin, X. K. Wu, H. Zhao, J. P. Lai, B. L. Huang and L. Wang, *J. Mater. Chem.*, 2020, **8**, 2323.
36 H. Ooka, J. Huang and K. S. Exner, *Front. Energy Res.*, 2021, **9**, 654460.
37 V. Stamenkovic, B. S. Mun, K. J. J. Mayrhofer, P. N. Ross, N. M. Markovic, J. Rossmeisl, J. Greeley and J. K. Nørskov, *Angew. Chem., Int. Ed.*, 2006, **45**, 2897.
38 L. Zhang, P. Lu, M. Yin, R. Li, B. Wang, X. Ma, M. Jiao, W. Ma and Z. Zhou, *Rare Met.*, 2024, DOI: **10.1007/s12598-024-03039-3**.
39 W. Y. Ming, P. Y. Sun, Z. Zhang, W. Z. Qiu, J. G. Du, X. K. Li, Y. M. Zhang, G. J. Zhang, K. Liu, Y. Wang and X. D. Guo, *Int. J. Hydrogen Energy*, 2023, **48**, 5197.
40 R. Ding, R. Wang, Y. Ding, W. J. Yin, Y. D. Liu, J. Li and J. G. Liu, *Angew. Chem.*, 2020, **132**, 19337.
41 R. Ding, W. J. Yin, G. Cheng, Y. W. Chen, J. K. Wang, X. B. Wang, M. Han, T. R. Zhang, Y. L. Cao, H. M. Zhao, S. P. Wang, J. Li and J. G. Liu, *ACS Appl. Mater.*, 2022, **14**, 8010.
42 N. S. Vasile, A. H. A. M. Videla and S. Specchia, *Chem. Eng. J.*, 2017, **322**, 722.
43 P. T. Sun, S. Zhou, Q. Y. Hu and G. P. Liang, *Commun. Comput. Phys.*, 2012, **11**, 65–98.
44 K. Suzuki, T. Toyao, Z. Maeno, S. Takakusagi, K. Shimizu and I. Takigawa, *ChemCatChem*, 2019, **11**, 4537.
45 X. Liu, M. Chen, J. Ma, J. Liang, C. Li, C. Chen and H. He, *China Powder Sci. Technol.*, 2024, **30**, 35.
46 F. Wang, C. Kuang, Z. Zheng, D. Wu, H. Wan, G. Chen, N. Zhang, X. Liu and R. Ma, *Chin. Chem. Lett.*, 2024, 109989.
47 Y. Ji, Z. Yu, L. Yan and W. Song, *China Powder Sci. Technol.*, 2023, **29**, 100.
48 W. Liu, W. Liu, T. Hou, J. Ding, Z. Wang, R. Yin, X. San, L. Feng, J. Luo and X. Liu, *Nano Res.*, 2024, **17**, 4797.
49 J. Ding, S. Jing, C. Yin, C. Ban, K. Wang, X. Liu, Y. Duan, Y. Zhang, G. Han, L. Gan and J. Rao, *Chin. Chem. Lett.*, 2023, **34**, 107899.
50 J. Li, S. Yan, G. Li, Y. Wang, H. Xu and G. Duan, *China Powder Sci. Technol.*, 2023, **29**, 101.
51 T. Onsree and N. Tippayawong, *Renewable Energy*, 2021, **167**, 425.
52 Q. J. Song, H. Y. Jiang and J. Liu, *Expert Syst. Appl.*, 2017, **81**, 22.
53 H. K. Esfeh, A. Azarafza and M. K. A. Hamid, *RSC Adv.*, 2017, **7**, 32893.
54 J. Sun, G. Zhang, T. Guo, G. B. Che, K. Jiao and X. R. Huang, *Appl. Therm. Eng.*, 2020, **165**, 114589.
55 M. Tian, S. Shi, Y. Shen and H. M. Yin, *Electrochim. Acta*, 2019, **293**, 390.
56 I. Blankenau, L. Marten and X. Li, *ECS Meet. Abstr.*, 2019, **36**, 1677.
57 C. C. Ngetich, J. Mutua, P. Kareru, K. Karanja and E. Wanjuru, *Fuel Cells*, 2023, **23**, 324–337.
58 Z. G. Zhao, D. J. Li, X. P. Xu and D. C. Zhang, *Energies*, 2023, **16**, 2167.
59 D. E. Glass and G. K. S. Prakash, *Electroanalysis*, 2019, **31**, 718.
60 D. E. Glass, G. A. Olah and G. K. S. Prakash, *J. Power Sources*, 2017, **352**, 165.
61 X. H. Yan, P. Gao, G. Zhao, L. Shi, J. B. Xu and T. S. Zhao, *Appl. Therm. Eng.*, 2017, **126**, 290.
62 Z. Chen, S. Mak, C. F. J. Wu and J. Am, *Stat. Assoc.*, 2023, 1–14.
63 J. Yang, F. Zhang and J. Chen, *China Powder Sci. Technol.*, 2024, **30**, 161.
64 K. Chen, D. Ma, Y. Zhang, F. Wang, X. Yang, X. Wang, H. Zhang, X. Liu, R. Bao and K. Chu, *Urea Adv. Mater.*, 2024, **36**, 2402160.
65 A. Fumiaki and T. Keisuke, *Energy Mater.*, 2024, **4**, 400006.
66 G. Lu, G. Meng, Q. Liu, L. Feng, J. Luo, X. Liu, Y. Luo and P. K. Chu, *Adv. Powder Mater.*, 2024, **3**, 100154.
67 S. Chen, G. Qi, R. Yin, Q. Liu, L. Feng, X. Feng, G. Hu, J. Luo, X. Liu and W. Liu, *Nanoscale*, 2023, **15**, 19577.
68 B. W. Wang, G. B. Guo, H. Z. Wang, J. Xuan and K. Jiao, *Energy AI*, 2020, **1**, 100004.
69 X. Kang, Y. J. Wang, C. Jiang and Z. H. Cheng, *Batteries*, 2024, **10**, 242.
70 H. Kim, S. Hong, J. Bang, Y. Jun, S. Choe, S. Kim and S. Ahn, *Energy Mater.*, 2024, **4**, 400010.
71 B. He, Y. Ling, Z. Wang, W. Gong, Z. Wang, Y. Liu, T. Zhou, T. Xiong, S. Wang, Y. Wang, Q. Li, Q. Zhang and L. Wei, *eScience*, 2024, **4**, 100293.
72 H. Fan, K. Liu, X. Zhang, Y. Di, P. Liu, J. Li, B. Hu, H. Li, M. Ravivarma and J. Song, *eScience*, 2024, **4**, 100202.